Iterative estimation of coherent-scattering profiles from given positions by use of a single-direction beam

doi: 10.1007/s12194-012-0159-0

Iterative estimation of coherent-scattering profiles from given positions by use of a single-direction beam

Mitsuaki Terabe[1,2]**, Hiroyuki Okamoto**[1]**, and Kichiro Koshida**[1]

[1]Division of Health Sciences, Graduate School of Medical Science, Kanazawa University, 5-11-80, Kodatsuno, Kanazawa, Ishikawa 920-0942, Japan

[2]Department of Radiology, Toyohashi Municipal Hospital, 50, Hakken-nishi, Aotake, Toyohashi, Aichi, 441-8570, Japan

Corresponding author

Mitsuaki Terabe

E-mail: mi.terabe@gmail.com

Tel: 81-532-33-6111

Keywords

Coherent scatter, X-ray diffraction, Successive approximation, Iterative reconstruction

Abstract

The coherent scattering distribution is useful for characterization of materials in the medical field, and obtaining this information from a given position in the object is a useful new diagnostic approach. We propose a simpler geometric approach, which requires only a single-direction X-ray beam with no collimator in front of the detector. This method iteratively estimates coherent scattering profiles from given positions along the beam path, based on the projections positioned at different object-to-detector distances. We confirmed the proposed calculation algorithm by numerical simulation and performed a simple experiment including attenuation correction. The accuracy of matching with the original profiles was dependent on the number of iterations, the distance between the first and second detectors, the distance between two objects, and the shape of the scattering profile. Whereas multiple scattering was the main problem in the experiment, the calculated scattering profiles matched well with the original profile. This technique indicates the feasibility of developing a coherent-scatter imaging system.

1 Introduction

Coherent scatter is based on the interference of scattered X-rays from different electrons in the object material. This interference caused by the differences in interatomic or intermolecular distances exhibits characteristic scattering patterns, which are commonly used for the study of the material structure in crystallographic analysis. Amorphous materials, such as biological tissue, show relatively broad scattering patterns that dependent on the average intermolecular spacing, but can still reveal the characteristics of the material.

In the medical field, coherent scatter has attracted a great deal of attention mainly because of its capability for characterization of materials. Many investigators have attempted to obtain useful information by using this technique.

Breast tissue is one of the most promising targets for the coherent-scatter technique. Many authors have demonstrated differences between normal and diseased breast tissues [1-6], and various classification models have been developed for differential diagnosis between benign and malignant lesions [7-10]. Furthermore, in the case of fibroglandular breast tissue and carcinoma as imaging targets, the low-angle scatter model has a higher signal-to-noise ratio than does the primary model, which is the

conventional imaging method, with selection of optimum momentum transfer arguments [11].

Another potential target of interest in medical use is bone. Coherent scatter can be used for distinguishing between the fat and mineral components of bone, which is useful for diagnosis of diseases involving bone demineralization [12-15]. Whereas current clinical methods for examination of bone mineral density are susceptible to errors due to variable fat content and density, the coherent scatter technique can distinguish between bone constituents, including collagen and water components, with greater precision [16].

Urinary stone analysis [17-19] and discrimination between normal and cancerous liver tissue [14] have also been studied as possible medical applications of coherent scattering.

The availability of coherent scatter in the medical field has been reported as described above. Visualizing this information on two-dimensional (2D) or three-dimensional (3D) images would be more useful for clinical use, and several imaging approaches to this have been attempted.

Tomographic imaging by use of the angular distribution of coherent scattering as the projection data set was proposed by Harding et al. [20, 21]. They used a conventional

polychromatic X-ray source and applied the geometry of first-generation computed tomography (CT), *i.e.*, pencil-beam scanning geometry. Subsequently, similar approaches were used for adapting coherent-scatter CT for medical applications [16, 18, 19, 22-24]. Schlomka et al. [25] advanced the coherent-scatter CT techniques by applying fan-beam geometry for acquisition of coherent-scatter CT projection data to reduce the exposure time, with algebraic reconstruction. Stevendaal et al. [26] subsequently introduced 3D filtered back-projection to reduce the computation time. Although these fan-beam geometry techniques can reduce the exposure time, the patient exposure dose is increased by placement of a collimator in front of the detector, because this collimator reduces the azimuthal angular scatter of photons.

The performance of coherent scatter imaging is largely dependent on the angular resolution. The factors that mainly affect the angular resolution are the energy spectral width and the beam divergence (focal spot size and beam width) [27]. Therefore, monoenergetic or quasi-monoenergetic X-rays with balanced filters [27] and highly parallel X-ray beams are suitable for coherent-scatter imaging. In general, it is difficult to rotate these X-ray sources because of the need to maintain an accurate setting of the monochromatic system and a sufficient distance between the source and the object for beam parallelism. Rotating the patient is also impossible in clinical use.

Here, we propose a method for estimating coherent-scattering profiles from given positions along the beam path by use of two projections acquired at different object-to-detector distances. This method requires only a single-direction X-ray beam and no collimation in front of the detector, whereas 2D plane pencil-beam scanning is required for 3D acquisition. We describe the details of this method, and we present numerical simulations and a phantom experiment with attenuation correction as the basic one-dimensional (1D) geometry by use of a synchrotron radiation source.

2 Materials and methods

In conventional X-ray imaging based on X-ray attenuation, the single-direction transmission beam through the patient cannot provide positional information along the beam path. Therefore, many different directions of beams are required for the acquisition of positional information.

However, in coherent-scatter imaging, the scattering distributions projected to the detector can be caused to vary by changing the distance between the object and the detector, because the scattering proceeds at various angles. Thus, we thought it possible to estimate the scattering position along the beam path by connecting two

same-intensity scatters from two projections acquired at different object-to-detector distances (Fig. 1). Actually, it is difficult to solve this problem analytically because the projection data result from the convergence of scatterings that have many different intensities and angles. Thus, we attempted to estimate the scattering profiles from given positions by successive approximations.

2.1 Projection process of coherent scattering

The approach presented is based on angular dispersive coherent scattering with a synchrotron monochromatic beam.

The differential coherent-scattering cross-section of polarized X-rays is

$$\frac{\mathrm{d}\sigma_{\mathrm{coh}}}{\mathrm{d}\Omega} = r_0^2 \left(1 - \sin^2\theta\cos^2\phi\right) F^2(x), \qquad (1)$$

where r_0^2 is the classical electron radius, θ is the scattering angle, ϕ is the azimuthal angle, and $F^2(x)$ is the molecular form factor that is dependent on the momentum transfer $x = (1/\lambda)\sin(\theta/2)$, where λ is the X-ray wavelength (Fig. 2). According to Kleuker et al. [23], the variations of scattering intensity dependent on the azimuthal angle are negligible for small scattering angles. The results of our preliminary experiment at 25 keV indicated that the differences in the scattering intensity profile

between $\phi = 0°$ and $\phi = 90°$ were less than 1% on average at $\theta < 15°$. Therefore, we did not consider the dependence of the azimuthal angle of the scattering intensity. Most biological tissues are amorphous or polycrystalline, and such tissues produce azimuthally symmetric scattering patterns [24]. The scattering profiles that we expect would thus be 1D profiles that are dependent only on the scattering angle.

Low-angle scattering is dominated by single coherent scattering rather than single Compton scattering and multiple scattering [21]. Therefore, we consider only single coherent scattering below for simplicity.

The acquisition of projection data for coherent scattering follows from the work of Harding et al. [21]. The geometry for this study is shown schematically in Fig. 3a. Actually, scattering is projected onto the detector as a 2D distribution such as that in Fig. 2, but we treat these projection data as an azimuthally averaged 1D scattering profile here. We acquire the projection data by positioning the detector at two different distances from the original point, L_1 and L_2. In the calculation, we partition the scattering angle into a given interval $\Delta\theta$, set the scattering (calculation) point l_n at given intervals of Δl, and define the closest point in the object to the detector l_0 as the original point. The number of photons N_{mn} scattered into a fixed angle $\Delta\theta$ derived from position l_n in the object toward angle θ_m is given by

$$N_{mn} = N_0 \frac{N_A \rho}{M} \alpha(l_n) \beta(l_n, \theta) \int_{\theta_m}^{\theta_m + \Delta\theta} \frac{d\sigma_{coh}}{d\Omega} d\theta, \quad (2)$$

where N_0 is the number of incident X-ray photons, N_A is Avogadro's number, ρ is density, M is molecular weight, and $\alpha(l_n)$ and $\beta(l_n, \theta)$ are the self-attenuation factors before and after the scattering point, respectively (Fig. 3b).

By measurement of the transmission beam and the object thickness, we can determine the attenuation coefficient along the beam path. However, in the proposed method, it is impossible to determine the attenuation coefficients for all positions, as in CT; thus, we assume that the attenuation coefficient along the beam path is constant. The attenuation coefficient calculated by a transmission measurement through the object is μ, the total thickness of the object is W, and the distance from the scattering point to the origin is $l_n = \Delta l \times n$. Thus, the attenuation factors are

$$\alpha(l_n) = \exp[-\mu(W - l_n)] \quad (3)$$

and

$$\beta(l_n, \theta) = \exp\left\{ -\mu \left[\frac{l_n}{\cos\theta_m} + \frac{l_n}{\cos(\theta_m + \Delta\theta)} \right] \Big/ 2 \right\}. \quad (4)$$

In the proposed method, the scattering angle is built into the calculation as $\Delta\theta$, which has a range, and therefore the distance of the scattering path is used as the average.

We also partition the detector into given intervals ΔD, and then the total number of X-ray photons Y_i scattered into the detector elements D_i is given by

$$Y_i = \sum_{j=1}^{J} N_j P_{ij}, \quad (5)$$

where $N_j (j = m \times n) = N_{mn}$, P_{ij} is the probability for the number of X-ray photons N_j incident into the detector element D_i. P_{ij} is represented by two factors, *i.e.*, the geometry factor G_{ij} and the distance attenuation factor H_{ij}:

$$P_{ij} = G_{ij} \times H_{ij}. \quad (6)$$

The geometry factor is defined as the ratio between the distance at the detector plane projected by the scattering angle $\Delta\theta$ and the distance of the detector element ΔD, as expressed below:

$$G_{ij} = \frac{\Delta D_i}{\left|\tan(\theta_m + \Delta\theta) \times (l_n + L) - \tan\theta_m \times (l_n + L)\right|}. \quad (7)$$

Of course, the case in which the detector plane projected by the scattering angle $\Delta\theta_m$ does not overlap with the detector element G_{ij} must be zero. The number of scattered photons reaching the detector element decreases with the distance of this element to the scattering point, in accordance with the inverse-square law [26]. Therefore, the distance attenuation factor is given by

$$H_{ij} = \left\{ (l_n + L)^2 + \left[\frac{\tan\theta_m \times (l_n + L) + \tan(\theta_m + \Delta\theta) \times (l_n + L)}{2} \right]^2 \right\}^{-1}, \quad (8)$$

where the distance of the scattering path is used as the average in common with the attenuation factor in equation (4).

2.2 Iterative estimation

The maximum-likelihood expectation maximization algorithm (ML-EM) was first applied to image reconstruction in emission tomography by Shepp and Vardi [28]. This algorithm is an iterative method, where a given image is first assumed, and the differences between the projection data calculated from this image and the actual measurements are then iteratively minimized.

We apply this algorithm in our method, and we begin the calculation with the initial estimated values N_j^k. The next estimate is given by

$$N_j^{k+1} = \frac{N_j^k}{\sum_{i=1}^{I} P_{ij}} \sum_{i=1}^{I} \frac{y_i P_{ij}}{\sum_{j'=1}^{J} N_{j'}^k P_{ij'}}, \qquad (9)$$

where y_i represents the measured projection data. The projection data acquired at different positions along the beam path are built into the algorithm, and the iterative calculation is performed.

2.3 Numerical simulations

2.3.1 Point object model

To confirm the proposed algorithm, we simulated a numerical model consisting of two materials: water and fat. In this simulation, we assumed that these two materials had no thickness and that the X-ray photons were not attenuated. Therefore, we did not use the self and distance attenuation correction in equations (3), (4), and (8). The coherent scattering form factors for simulation data were taken from the study by Peplow and Verghese [29].

We also performed a simulation with two other materials: polycarbonate (PC) and polyethylene (PE). These materials are amorphous, similar to water and fat, and therefore scattering does not depend on the azimuthal angle. The scattering profiles of these materials were taken from the study by Kosanetzky et al. [30].

Many medical applications using coherent scatter have treated mainly two types of components as the target, *i.e.*, bone and fat components [13-15], water and fat components, or healthy and malignant components [1, 2, 4-6, 10, 31, 32]. Therefore, we treated two material pairs in the present study.

To evaluate the match between the input profile and the calculated profile, we used the Pearson correlation coefficient, which was calculated with the CORREL function in Microsoft Excel in the numerical simulations and in the experiment.

2.3.2 Volume object model

A real object as the target for this application has thickness. We constructed a simple volume object consisting of PC and PE by setting the scattering point with small gaps along the beam path. The scattering points were set at 0 mm to 10 mm from the original point for PC and 10 mm to 20 mm from the original point for PE at intervals of 2 mm. Similar to the point-object model, this model also did not simulate the self and distance attenuation.

2.4 Experiment

We performed an experiment on the 10-mm thick PC and PE plates in the same way as described in section 2.3.2 to evaluate the capability of our method, including the attenuation correction.

The experiment was performed at beamline BL-15B1 of the Photon Factory in the High Energy Accelerator Research Organization (KEK-PF), Japan. Polychromatic X-rays from the synchrotron radiation source were monochromatized at 25 keV by a Si(111) double-crystal monochromator. The monochromatic X-rays were collimated by

slit systems 1 × 1 mm in cross-sectional area. The detector was a 20 cm × 25 cm imaging plate (BAS-SR 2025; Fuji Photo Film Co. Ltd, Tokyo, Japan), and the scatter images obtained were scanned with a BAS-2500 Bio-Imaging Analyzer (Fuji Photo Film Co. Ltd, Tokyo, Japan).

The pixel values are the values after logarithmic conversion; thus, we converted pixel values into relative values proportional to the exposure dose. Images were analyzed with use of the "Radial Profile Plot" with the "Radial Profile Extended" plug-in of ImageJ (available from http://rsb.info.nih.gov/ij/). The "Radial Profile Plot" plug-in produces a profile plot of normalized integrated intensities around concentric circles as a function of distance from a given point. This area of the circle that is integrated can be defined arbitrarily by choosing the starting angle and the integration angle by the "Radial Profile Extended" plug-in. To decrease the statistical noise, we used a fan-shaped area (azimuthal angle of 5°). The 2D scatter images were converted to 1D projection data in this process. In addition, we replaced the measured projection data by 0 at less than 1° to avoid the effects of the primary beam [6].

We used a digital dosimeter (Solidose 308; RTI Electronics, Mölndal, Sweden) with a solid-state detector (R100; RTI Electronics, Mölndal, Sweden) for the transmission measurement. The incident dose and the dose transmitted through the object were

measured, and the attenuation coefficient was calculated.

3 Results and discussion

3.1 Numerical simulations

3.1.1 Point object model

Figure 4 shows the projection data simulated at L_1 = 120 mm and L_2 = 240 mm, with water set at the original point (l_0) and fat set at 20 mm from the original point (l_1). A shift in the peak position and broadening of the scattering profile were observed in the projection at L_2 = 240 mm in comparison to that at L_1 = 120 mm. These projection data were input into y_i in equation (9), and the iterative calculation was performed as the range of the scattering angle $\Delta\theta$ was 0.5° and the length of the detector element ΔD was 1 mm.

The results of the calculation with different numbers of iterations are shown in Fig. 5. The calculated scattering profile of l_0 (water) with 5 iterations had an error peak near the fat peak, and it differed substantially from the input water profile. This error of the

profile was improved by increasing the number of iterations. The calculated profile of l_1 (fat) also differed from the input profile when the number of iterations was low.

The correlation coefficients for the calculated and input profiles are shown in Fig. 6. The correlation coefficients of both materials were markedly increased by increasing the number of iterations to around 200, and then gradually converged. Therefore, the number of iterations required for convergence does not depend significantly on the type of material. However, the correlation coefficient of fat was higher than that of water up to around 200 iterations. We inferred that the sharpness of the peak in the fat profile matched with the input profile at low numbers of iterations. Therefore, use of a low number of iterations before convergence would affect the calculation accuracy for each material.

The rate of change of the correlation coefficient fell below 0.2% with 400 to 500 iterations. We defined this rate of change as the convergence point, and we calculated the scattering profiles to convergence in all following calculations.

Accurate matching of the calculated profile also depends on the relationship of the distance between the first and second detectors. We fixed the first detector at $L_1 = 120$ mm, and we varied the distance of the second detector L_2 from 130 to 270 mm at intervals of 10 mm and then calculated the correlation coefficients of the profiles. The

results indicated that a short distance between the first and second detectors led to inaccurate matching of the profiles, as shown in Fig. 7. This inaccuracy was due to the relatively small differences in the peak positions in the two projection data sets. However, too large an object-to-detector distance caused a reduction of scattered photons and ultimately an increase in the patient dose. The correlation coefficients of both materials were almost maximal at L_2 = 240 mm and remained at the same level thereafter. Therefore, we applied L_2 = 240 mm as the optimum condition.

To measure the positional resolution, we calculated profiles at L_1 = 120 mm and L_2 = 240 mm while varying the distance between two object points from 2 mm to 20 mm in intervals of 2 mm (Fig. 8a). The results showed that the larger the distance between two objects, the larger the correlation coefficient, and the water profile was less accurate than the fat profile up to 14 mm. The results of the same simulation with the PC and PE pair are shown in Fig. 8b, where the range of the scattering angle $\Delta\theta$ was 0.2° and the distance of the detector element ΔD was 0.4 mm, because the main peak of the PE profile cannot be resolved at $\Delta\theta$ = 0.5 and ΔD = 1 mm. For resolving the position of materials, the distances of 14 mm in the water and fat pair, and 6 mm in the PC and PE pair, were needed in the case that the level of material existence is 0.95 of the correlation coefficient.

The differences in the angle of each main peak between PC and PE (Fig. 8c) were smaller than the relationship between water and fat. Nevertheless, the correlation coefficients for PC and PE were larger than those for water and fat, especially when the distance between the two objects was short. This more accurate matching of the PC and PE pair was probably due to the sharpness of the peak in the input profile of PE. The sharpness of the peak was confirmed by the fact that the full width at half maximum (FWHM) of the main peak in the input PE profile was 0.25° and that of the fat profile was 2.1°. Therefore, it is expected that more crystalline materials, such as bones and urinary stones, would have a higher positional resolution due to the ease of localization of the scattering position.

3.1.2 Volume object model

We set five calculation points at the same interval in the computationally constructed volume object, followed by iterative calculation (Fig. 9). We defined the closest point to the detector in PC as the original point, and we set position A as 2 mm distant from the original point to the source side, with positions B, C, D, and E at intervals of 4 mm, as shown in Fig. 9f. The intensities of the calculated and input profiles are normalized to

the peak intensity of position E and the input PE profile, respectively.

The profile of position C at which both materials were in contact showed a shape that would be a mixture of each peak (Fig. 9c). The correlation coefficients of position C to the PC and PE profiles were 0.78 and 0.82, respectively (Fig. 9g).

The profiles of position A and position B were well matched with the input PC profile. Notably, position A, which was farthest from PE, had the highest correlation coefficient of 0.95. In addition, the profiles of position D and position E showed the same tendency. The correlation coefficient between the input PE profile and the profile of position E was 0.96.

The main peak heights of position C or position D, which were close to the other material side, were slightly low compared with the input profile. Moreover, the close point to the other material side showed an error peak that seemed to be an effect of this other material. However, we would be able to distinguish this error peak due to the shift of the peak angle.

3.2 Experiment

The experimental results calculated with the same points and parameters as in the

simulation (section 3.1.2) are shown in Fig. 10. Calculated profiles were compared with the scatter patterns reported by Kosanetzky et al. [30] as the pure original data for PC and PE. The intensities of the calculated and original profiles were normalized to the peak intensity of position E and the original PE profile, respectively.

Although the profile shapes of each point were almost the same as those in the simulation results shown in Fig. 9, the main peak area of position A was 32% lower than that of the original PC profile, and mismatches of the profiles on the high-angle side at position A and the low-angle side at position E were observed. These errors in the experiment would be due to the effects of attenuation and multiple scattering because the simulations do not include these effects.

The self-attenuation correction which used the attenuation coefficient 0.35 cm^{-1} at 25 keV was obtained from the transmission dose through PC and PE because a 2D attenuation map could not be obtained with our method (section 2.1). However, we corrected the self-attenuation by considering the distance passed through by the scattering photons in the object at each angle, and hence the difference in scattering intensity was only 0.16% (at position A and a scattering angle of 6°), compared with the case in which the respective attenuation coefficients (0.41 cm^{-1} for PC and 0.30 cm^{-1} for PE at 25 keV in our experiment) were used. Thus, it is unlikely that self-attenuation was

the main cause of the mismatches of the profiles in the experiment.

By analyzing the ratio between the projection estimated by calculation and the actually measured projection, we observed a relatively large difference at the second detector. Our method does not involve detection of the scattering at a specific angle by the collimator in front of the detector, but estimates the scattering according to the relative difference in the scattering distributions at two projections. Therefore, our method cannot distinguish multiple scattering from the beam path, and it recognizes this as incorrect angle scattering from the wrong position. In addition, these scatterings from out of the beam path are not corrected for by the distance attenuation correction in equation (8); thus, differences in projections would appear especially at the second detector, which is set at a relatively long distance from the object. Thus, the mismatches of the profiles in the experiment would be caused by the calculation error due to the mismatch of the projection data between the first and the second detector affected by multiple scattering. Thran et al. [33] attempted a multiple scatter correction in coherent-scatter CT. If we eliminate multiple scattering, detection of the photons with the same energy as incident X-ray by using the energy selective detector is better because multiple scattering results in loss of energy.

4 Conclusions

We evaluated our method by numerical simulations, changing the calculation parameters and conditions, and demonstrated its usefulness in an experiment by using a simple phantom. It was possible to acquire the scattering profiles at given positions along the beam path with only a single-direction X-ray beam in studying two pairs of materials. This technique confirms the feasibility of developing a coherent-scatter imaging system.

Acknowledgments

We thank Prof. K Mizuno and Mr. K Inoue for their support during the experiment. This study was approved by the High Energy Accelerator Research Organization, Japan and performed under proposal number 2010G531.

References

1. Evans SH, Bradley DA, Dance DR, Bateman JE, Jones CH. Measurement of

small-angle photon scattering for some breast tissues and tissue substitute materials. Phys Med Biol. 1991;36:7-18.

2. Kidane G, Speller RD, Royle GJ, Hanby AM. X-ray scatter signatures for normal and neoplastic breast tissues. Phys Med Biol. 1999;44:1791-802.

3. Poletti ME, Goncalves D, Mazzaro I. X-ray scattering from human breast tissues and breast-equivalent materials. Phys Med Biol. 2002;47:47-63.

4. Castro CRF, Barroso RC, Lopes RT. Scattering signatures for some human tissues using synchrotron radiation. X-ray Spectrom. 2005;34:477-80.

5. Cunha DM, Oliveira OR, Pérez CA, Poletti ME. X-ray scattering profiles of some normal and malignant human breast tissues. X-ray Spectrom. 2006;35:370-4.

6. Elshemey WM, Elsharkawy WB. Monte Carlo simulation of x-ray scattering for quantitative characterization of breast cancer. Phys Med Biol. 2009;54:3773-84.

7. Ryan EA, Farquharson MJ. Breast tissue classification using x-ray scattering measurements and multivariate data analysis. Phys Med Biol. 2007;52:6679-96.

8. Oliveira OR, Conceicao AL, Cunha DM, Poletti ME, Pela CA. Identification of neoplasias of breast tissues using a powder diffractometer. J Radiat Res (Tokyo). 2008;49:527-32.

9. Bohndiek SE, Royle GJ, Speller RD. An active pixel sensor x-ray diffraction

(APXRD) system for breast cancer diagnosis. Phys Med Biol. 2009;54:3513-27.

10. Elshemey WM, Desouky OS, Fekry MM, Talaat SM, Elsayed AA. The diagnostic capability of x-ray scattering parameters for the characterization of breast cancer. Med Phys. 2010;37:4257-65.

11. Leclair RJ, Johns PC. Optimum momentum transfer arguments for x-ray forward scatter imaging. Med Phys. 2002;29:2881-90.

12. Harding G, Newton M, Kosanetzky J. Energy-dispersive x-ray diffraction tomography. Phys Med Biol. 1990;35:33-41.

13. Royle GJ, Speller RD. Low angle x-ray scattering for bone analysis. Phys Med Biol. 1991;36:383-9.

14. Newton M, Hukins DW, Harding G. Bone composition measured by x-ray scattering. Phys Med Biol. 1992;37:1339-47.

15. Royle GJ, Speller RD. Quantitative x-ray diffraction analysis of bone and marrow volumes in excised femoral head samples. Phys Med Biol. 1995;40:1487-98.

16. Batchelar DL, Davidson MT, Dabrowski W, Cunningham IA. Bone-composition imaging using coherent-scatter computed tomography: assessing bone health beyond bone mineral density. Med Phys. 2006;33:904-15.

17. Dawson C, Horrocks JA, Kwong R, Speller RD, Whitfield HN. Low-angle X-ray

scattering signatures of urinary calculi. World J Urol 14 Suppl. 1996;1:S43-7.

18. Davidson MT, Batchelar DL, Velupillai S, Denstedt JD, Cunningham IA. Laboratory coherent-scatter analysis of intact urinary stones with crystalline composition: a tomographic approach. Phys Med Biol. 2005;50:3907-25.

19. Wignall GR, Cunningham IA, Denstedt JD. Coherent scatter computed tomography for structural and compositional stone analysis: a prospective comparison with infrared spectroscopy. J Endourol. 2009;23:351-7.

20. Harding G, Kosanetzky J, Neitzel U. Elastic scatter computed tomography. Phys Med Biol. 1985;30:183-6.

21. Harding G, Kosanetzky J, Neitzel U. X-ray diffraction computed tomography. Med Phys. 1987;14:515-25.

22. Westmore MS, Fenster A, Cunningham IA. Tomographic imaging of the angular-dependent coherent-scatter cross section. Med Phys. 1997;24:3-10.

23. Kleuker U, Suortti P, Weyrich W, Spanne P. Feasibility study of x-ray diffraction computed tomography for medical imaging. Phys Med Biol. 1998;43:2911-23.

24. Batchelar DL, Cunningham IA. Material-specific analysis using coherent-scatter imaging. Med Phys. 2002;29:1651-60.

25. Schlomka JP, Schneider SM, Harding G. Novel concept for coherent scatter X-ray

computed tomography in medical applications. Proc SPIE. 2000;4142:218-24.

26. Stevendaal UV, Schlomka JP, Grass M. Filtered back-projection reconstruction technique for coherent-scatter computed tomography. Proc SPIE. 2003;5032:1810-9.

27. Beath SR, Cunningham IA. Pseudomonoenergetic x-ray diffraction measurements using balanced filters for coherent-scatter computed tomography. Med Phys. 2009;36:1839-47.

28. Shepp LA, Vardi Y. Maximum likelihood reconstruction for emission tomography. IEEE Trans Med Imaging. 1982;1:113-22.

29. Peplow DE, Verghese K. Measured molecular coherent scattering form factors of animal tissues, plastics and human breast tissue. Phys Med Biol. 1998;43:2431-52.

30. Kosanetzky J, Knoerr B, Harding G, Neitzel U. X-ray diffraction measurements of some plastic materials and body tissues. Med Phys. 1987;14:526-32.

31. Theodorakou C, Farquharson MJ. The classification of secondary colorectal liver cancer in human biopsy samples using angular dispersive x-ray diffraction and multivariate analysis. Phys Med Biol. 2009;54:4945-57.

32. Pani S, Cook EJ, Horrocks JA, Jones JL, Speller RD. Characterization of breast

tissue using energy-dispersive X-ray diffraction computed tomography. Appl Radiat Isot. 2010;68:1980-7.

33. Thran A, Stevendaal UV, Schlomka JP. Multiple scatter correction in coherent scatter computed tomography. Proc SPIE. 2005;5923:59230 P1-P12.

Fig. 1 Basic concept of estimating coherent scattering profiles from given positions along the beam path.

Fig. 2 Scheme of the scattering projected to the 2D plane.

Fig. 3 a) Geometric scheme for acquiring projection data. l_n is the scattering (calculation) point, and the point in the object closest to the detector is the origin l_0. The projection data are acquired at two different positions. L_1 and L_2 are the distances from the origin to the first and second detectors, respectively. The distance of the detector element ΔD and the range of the scattering angle $\Delta\theta$ are the calculation parameters, which are adjusted to allow representation of the original shape of the material's profile. **b)** The beam path within the object for the calculation of self-attenuation.

Fig. 4 Projection data calculated at the first detector, L_1 = 120 mm, and the second detector, L_2 = 240 mm, in numerical simulations. These projections are based on the scattering profiles from the 20-mm gap of two point objects: water and fat. The length of the detector element ΔD is 1 mm in this case.

Fig. 5 Calculated scattering profiles of **a)** water and **b)** fat position after 5, 50, 100, and 500 iterations, compared with each input profile. The intensities are normalized to the peak intensity of the input profile for fat.

Fig. 6 Correlation coefficients for the calculated and input profiles of water and fat as a function of the number of iterations.

Fig. 7 Correlation coefficients for the calculated and input profiles of water and fat as a function of the distance L_2. The position of the first detector is fixed at L_1 = 120 mm.

Fig. 8 Correlation coefficients for the calculated and input profiles as a function of the distance between **a)** water and fat, **b)** PC and PE. **c)** The input profiles of PC and PE.

Fig. 9 a–e) Calculated scattering profiles (numerical simulation) at each position, compared with the input profiles of PC and PE. The intensities of the calculated and input profiles are normalized to the peak intensity of position E and the PE profile, respectively. **f)** The scheme of the object and calculation points. **g)** The correlation coefficients for the calculated and input PC or PE profiles with the calculation points.

Fig. 10 a–e) Calculated scattering profiles (experiment) at each position compared with the original profiles of PC and PE. The intensities of the calculated and original profiles are normalized to the peak intensity of position E and the PE profile, respectively.

Fig. 1

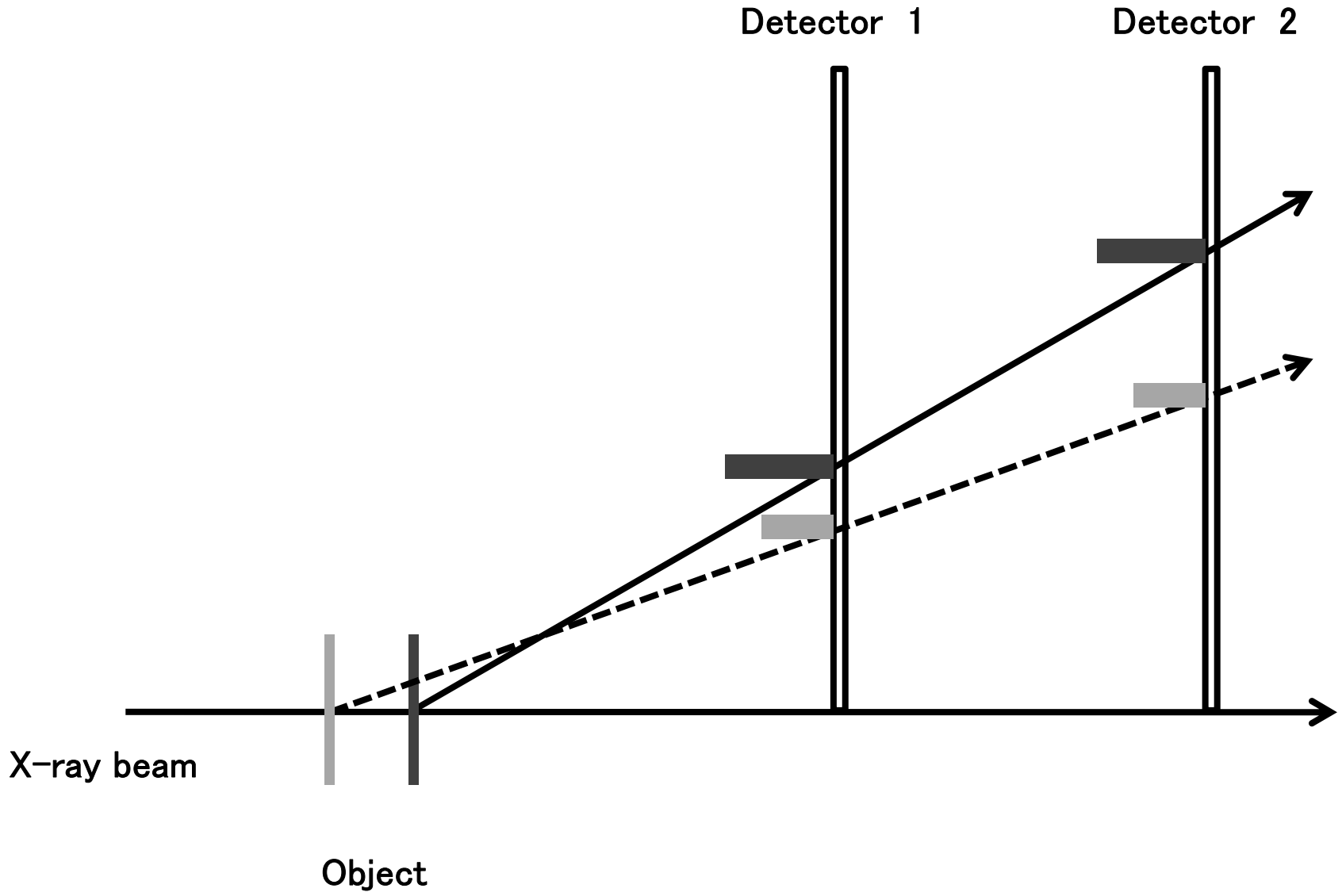

Fig. 2

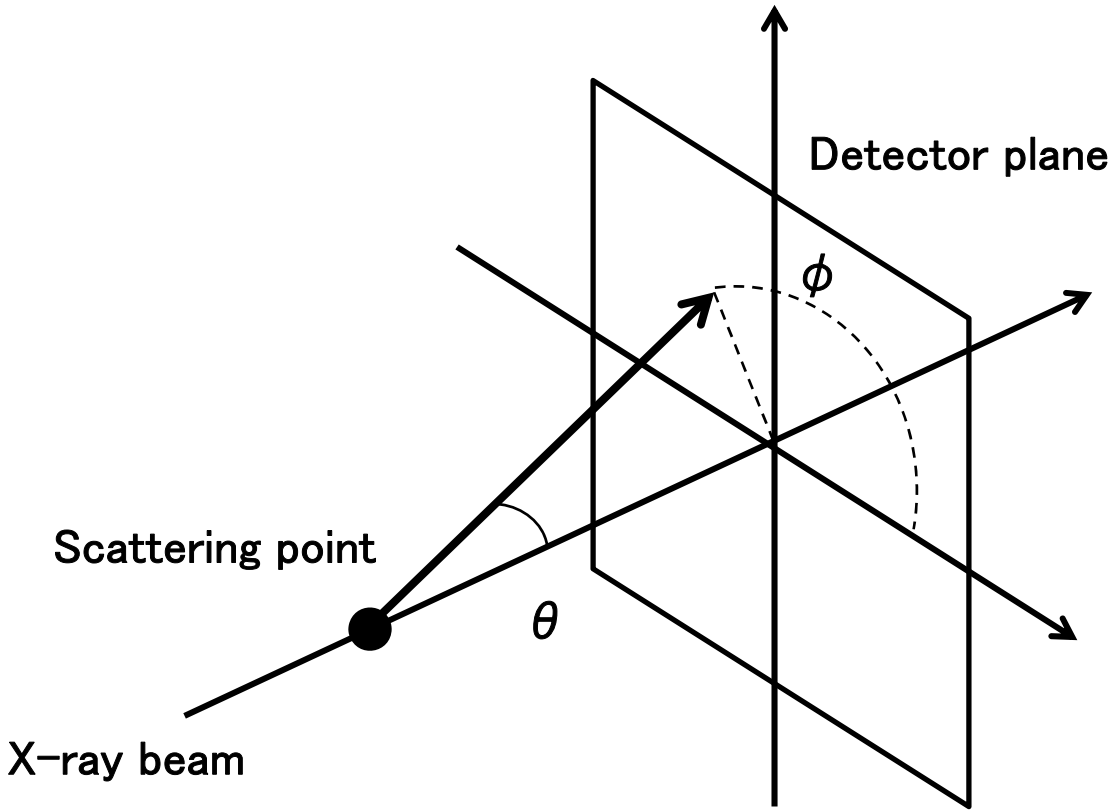

Fig. 3a

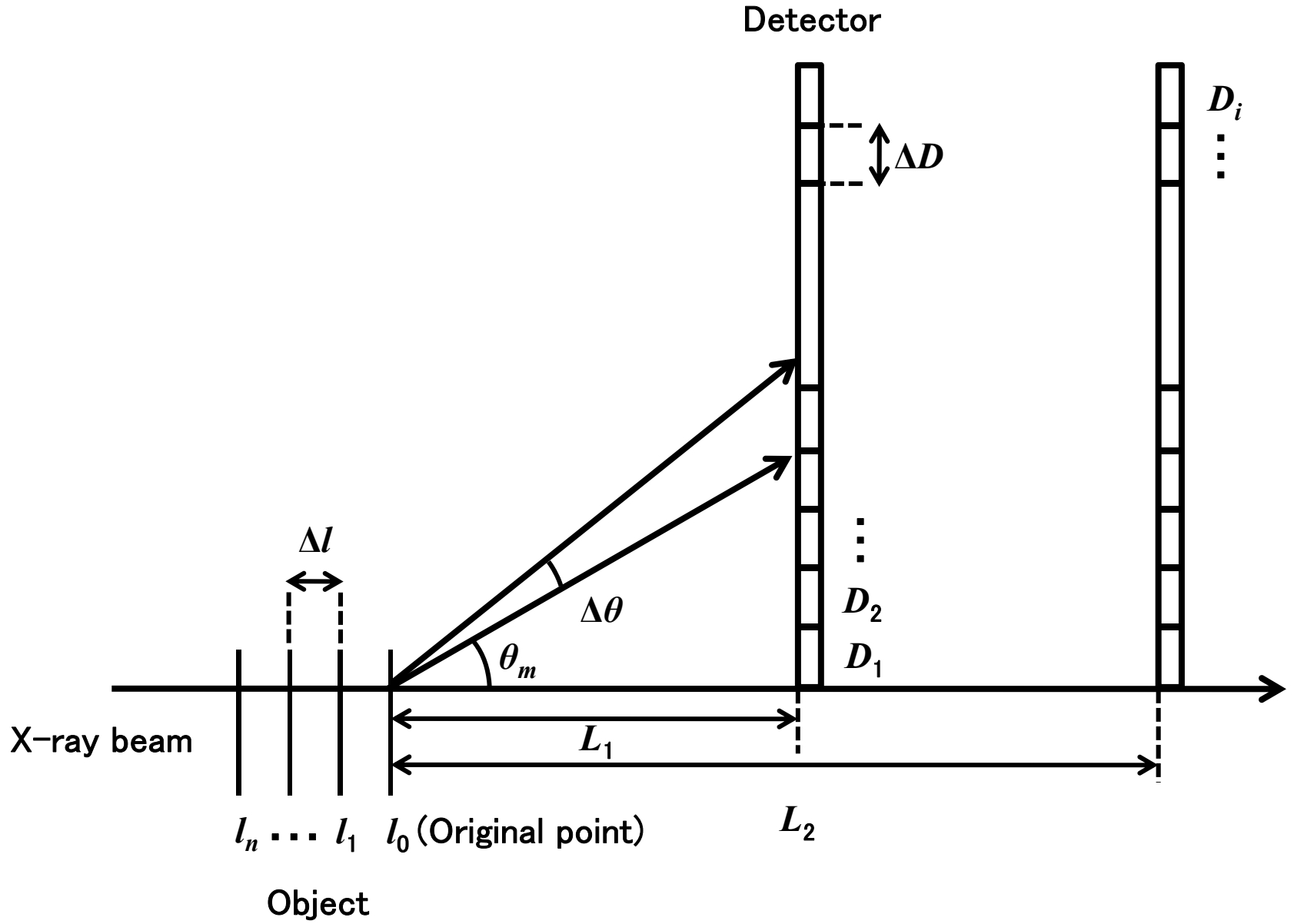
Detector
D_i
ΔD
Δl
$\Delta\theta$
θ_m
D_2
D_1
X-ray beam
L_1
L_2
l_n ... l_1 l_0 (Original point)
Object

Fig. 3b

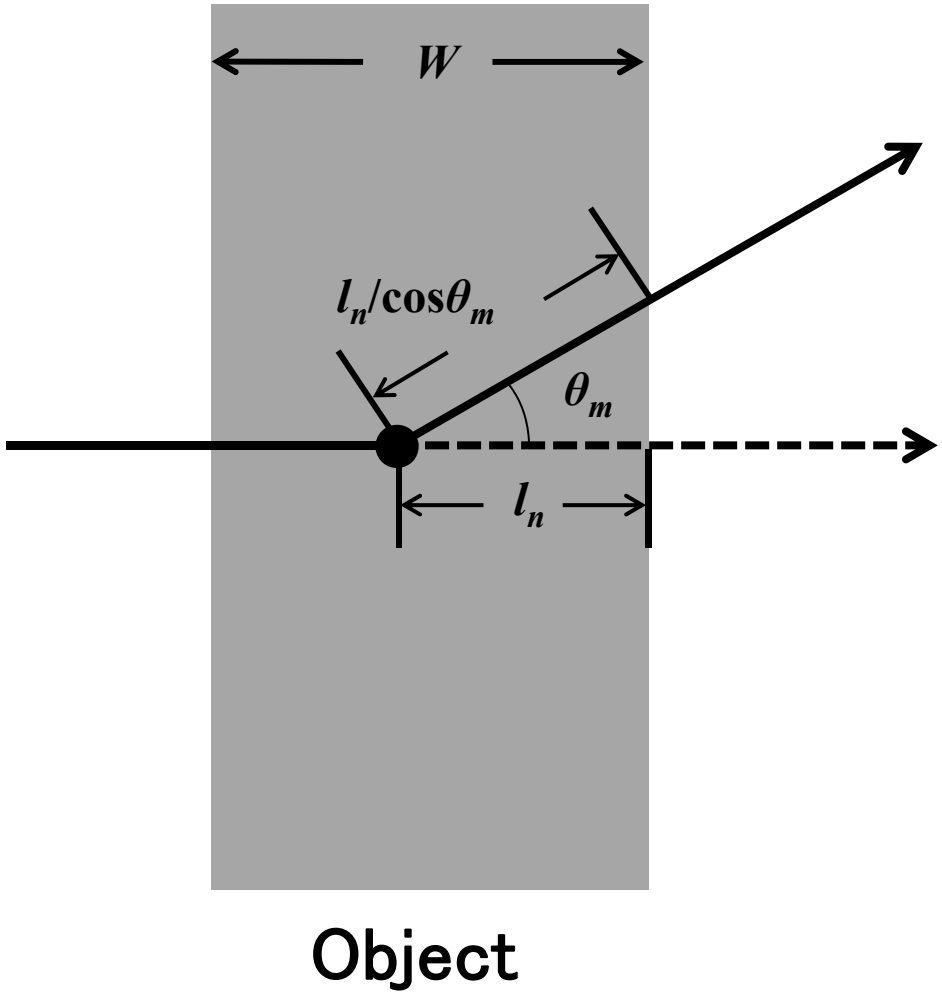

Fig. 4

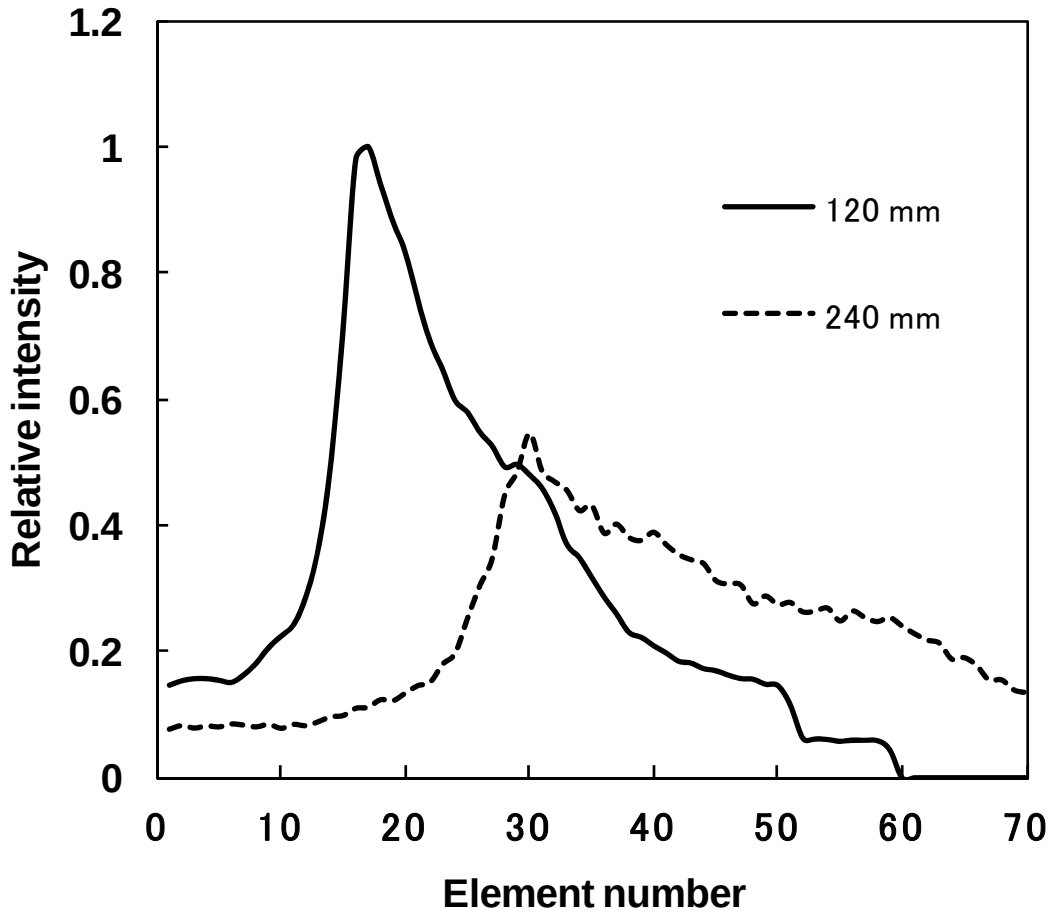
1.2
1
0.8
0.6
0.4
0.2
0
Relative intensity
120 mm
240 mm
0
10
20
30
40
50
60
70
Element number

Fig.5a

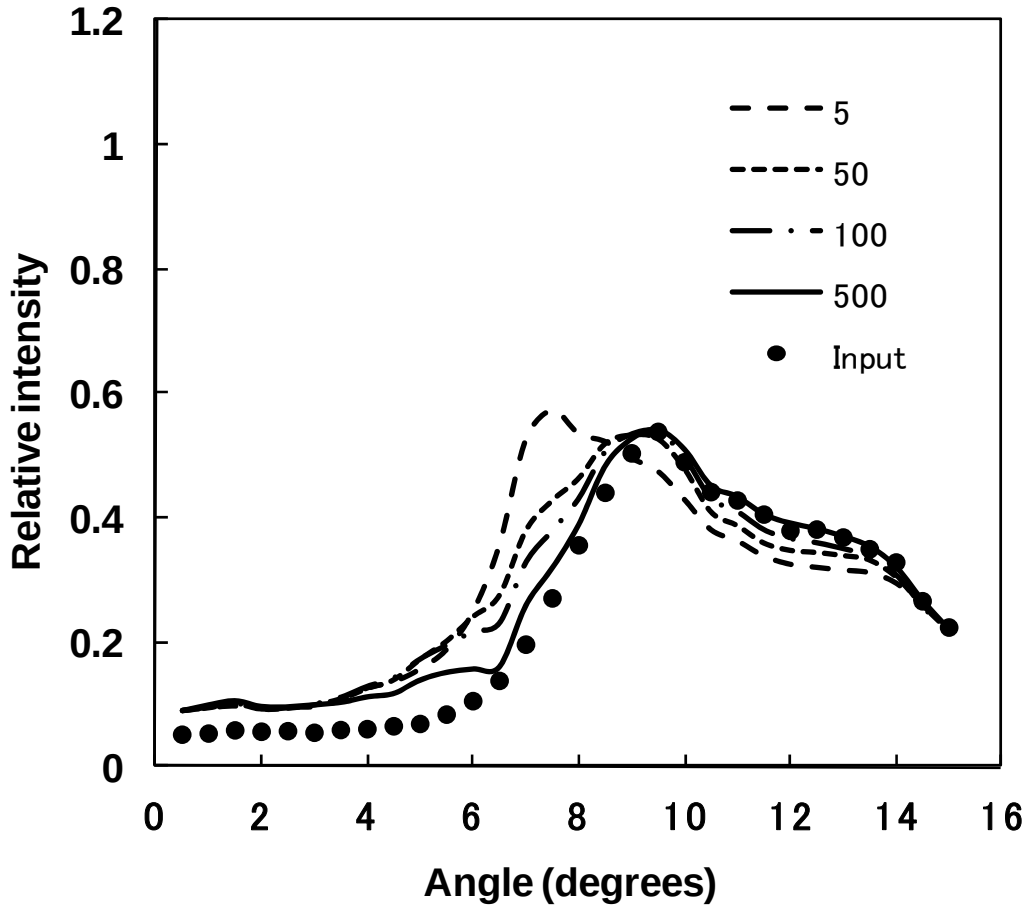
1.2
1
0.8
0.6
0.4
0.2
0
Relative intensity
0
2
4
6
8
10
12
14
16
Angle (degrees)
5
50
100
500
Input

Fig. 5b

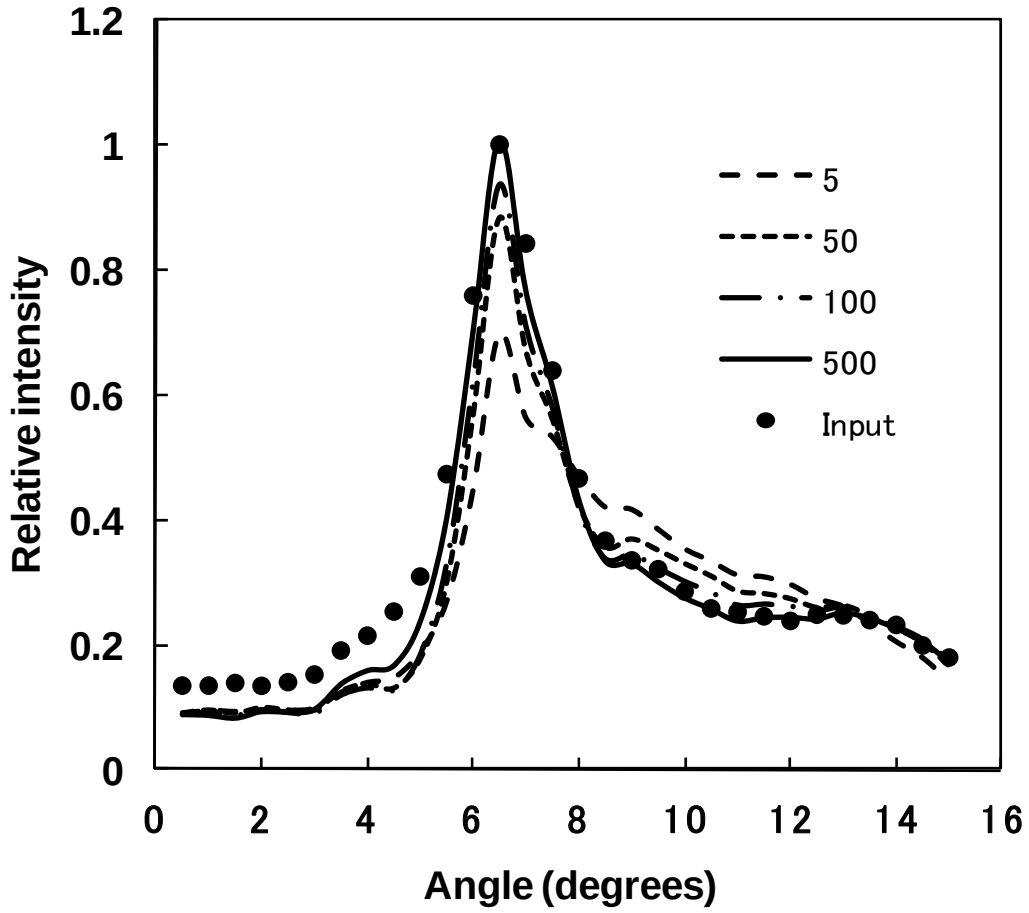
1.2
1
0.8
0.6
0.4
0.2
0
Relative intensity
0
2
4
6
8
10
12
14
16
Angle (degrees)
5
50
100
500
Input

Fig. 6

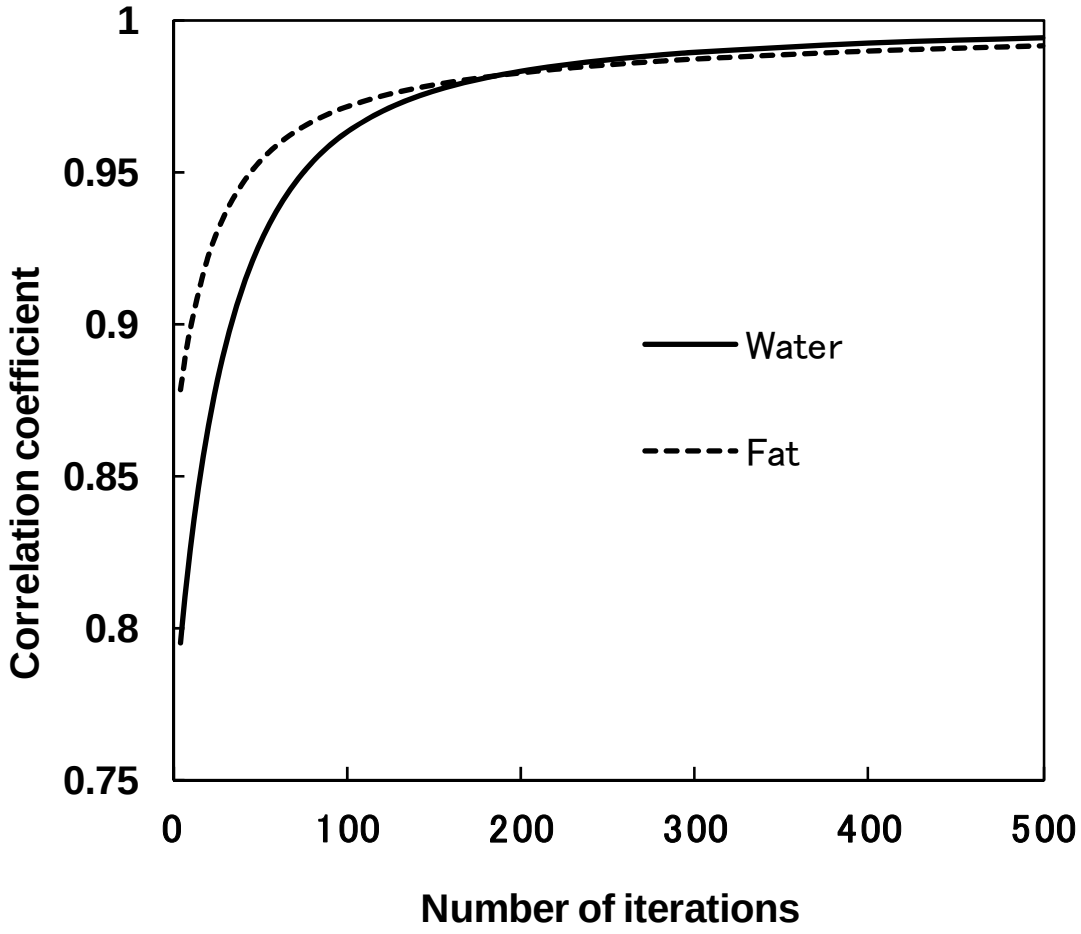
1
0.95
0.9
0.85
0.8
0.75
Correlation coefficient
0
100
200
300
400
500
Number of iterations
Water
Fat

Fig. 7

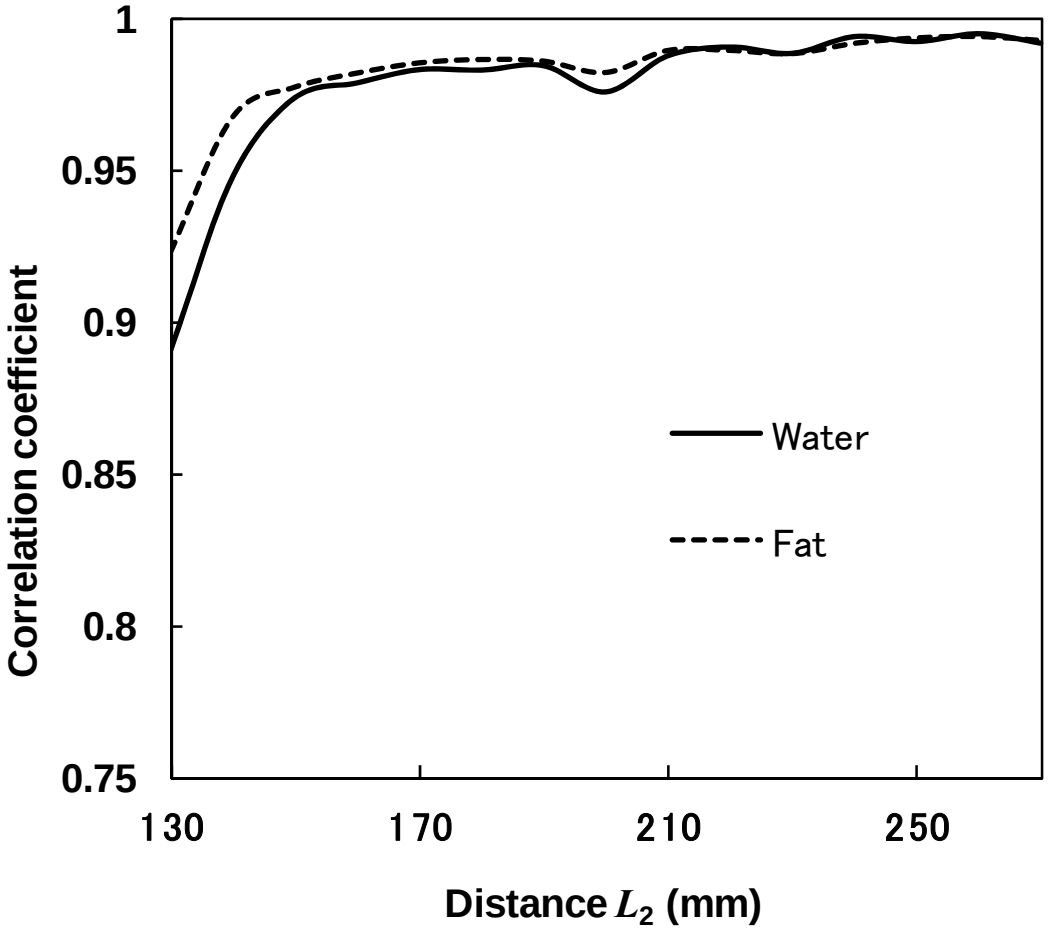
1
0.95
0.9
0.85
0.8
0.75
Correlation coefficient
130
170
210
250
Distance L_2 (mm)
Water
Fat

Fig. 8a

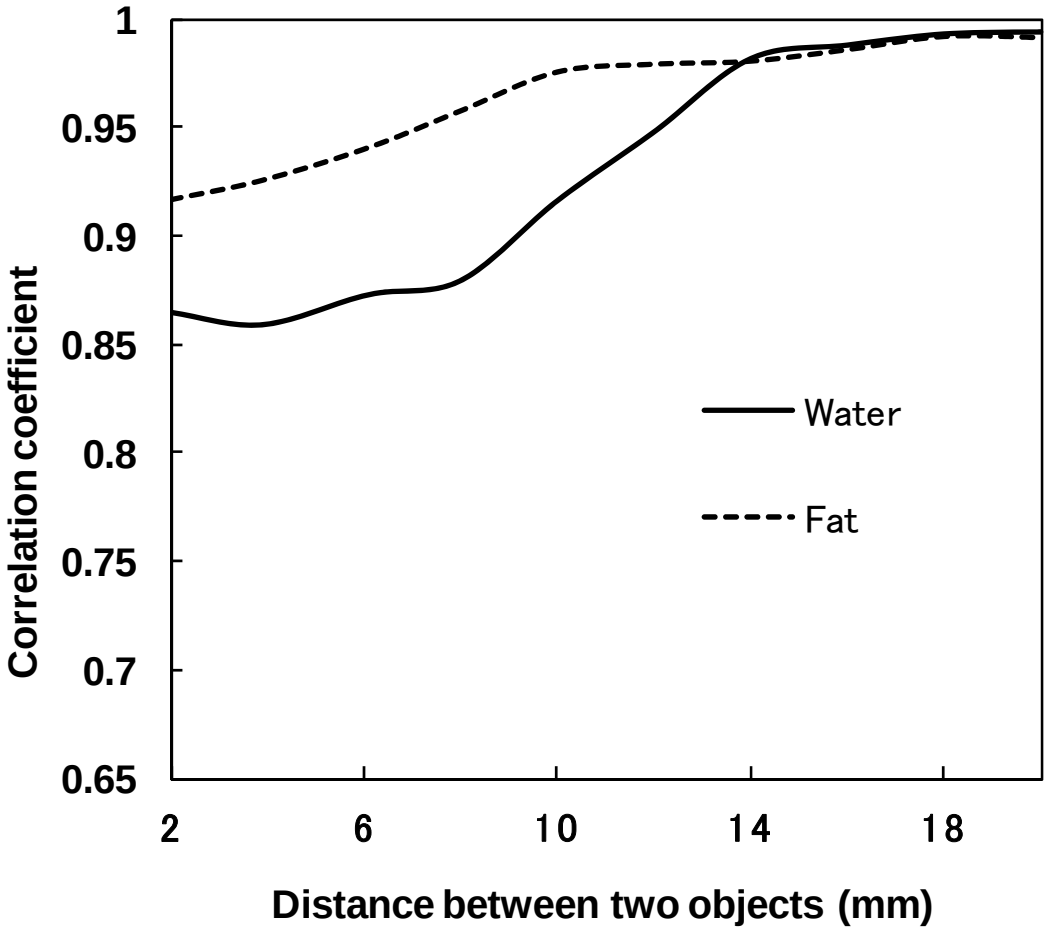
1
0.95
0.9
0.85
0.8
0.75
0.7
0.65
Correlation coefficient
2
6
10
14
18
Distance between two objects (mm)
Water
Fat

Fig. 8b

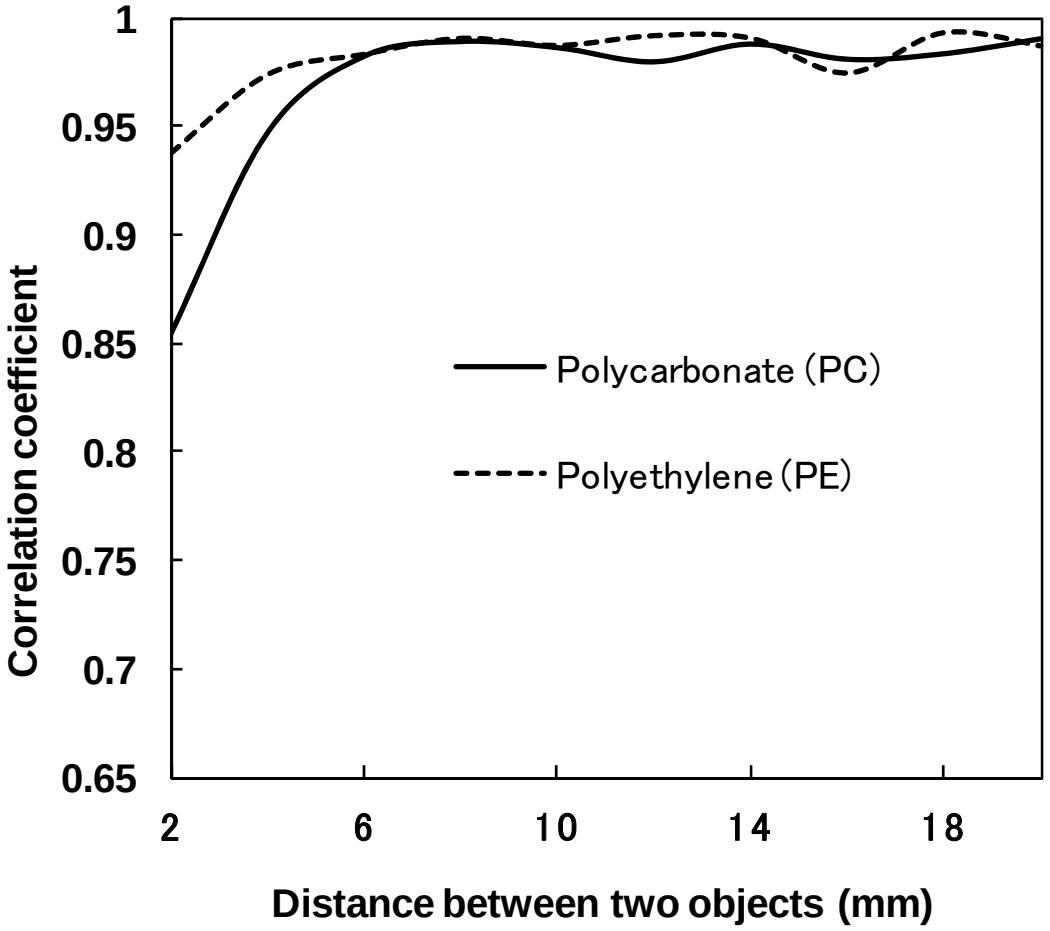
1
0.95
0.9
0.85
0.8
0.75
0.7
0.65
Correlation coefficient
2
6
10
14
18
Distance between two objects (mm)
Polycarbonate (PC)
Polyethylene (PE)

Fig. 8c

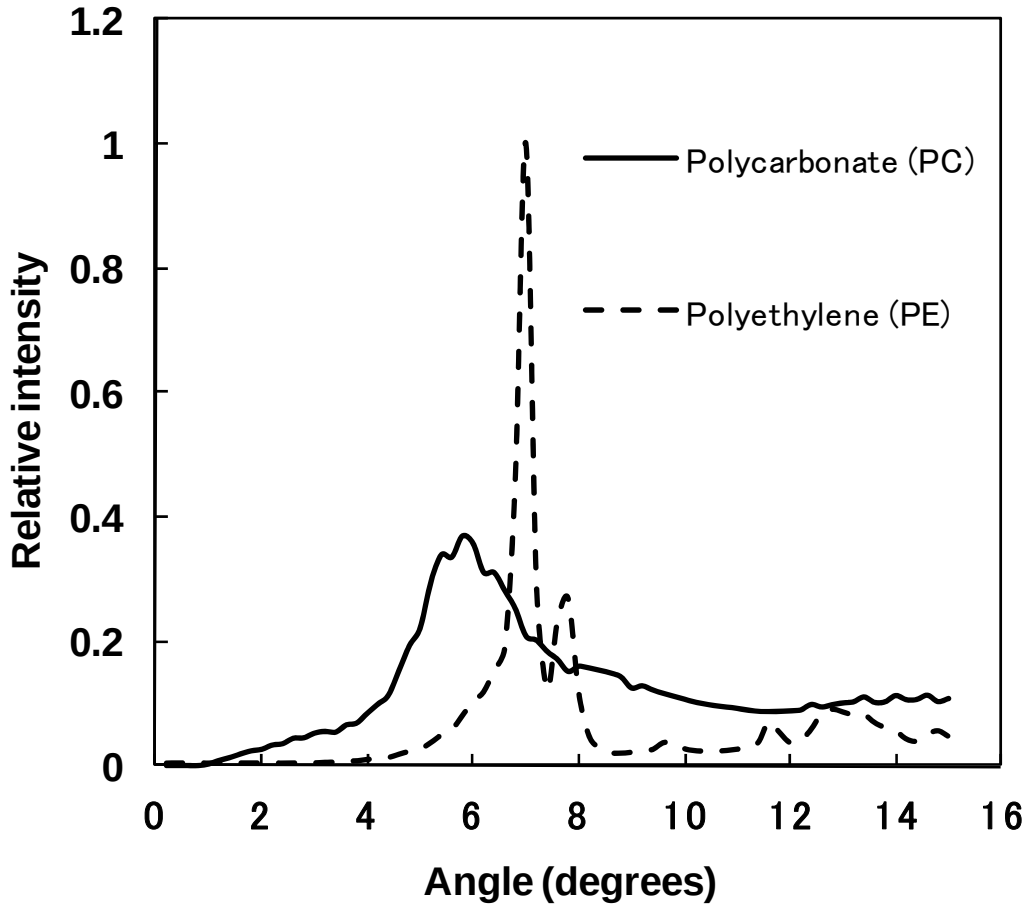
1.2
1
0.8
0.6
0.4
0.2
0
Relative intensity
0
2
4
6
8
10
12
14
16
Angle (degrees)
Polycarbonate (PC)
Polyethylene (PE)

Fig. 9a

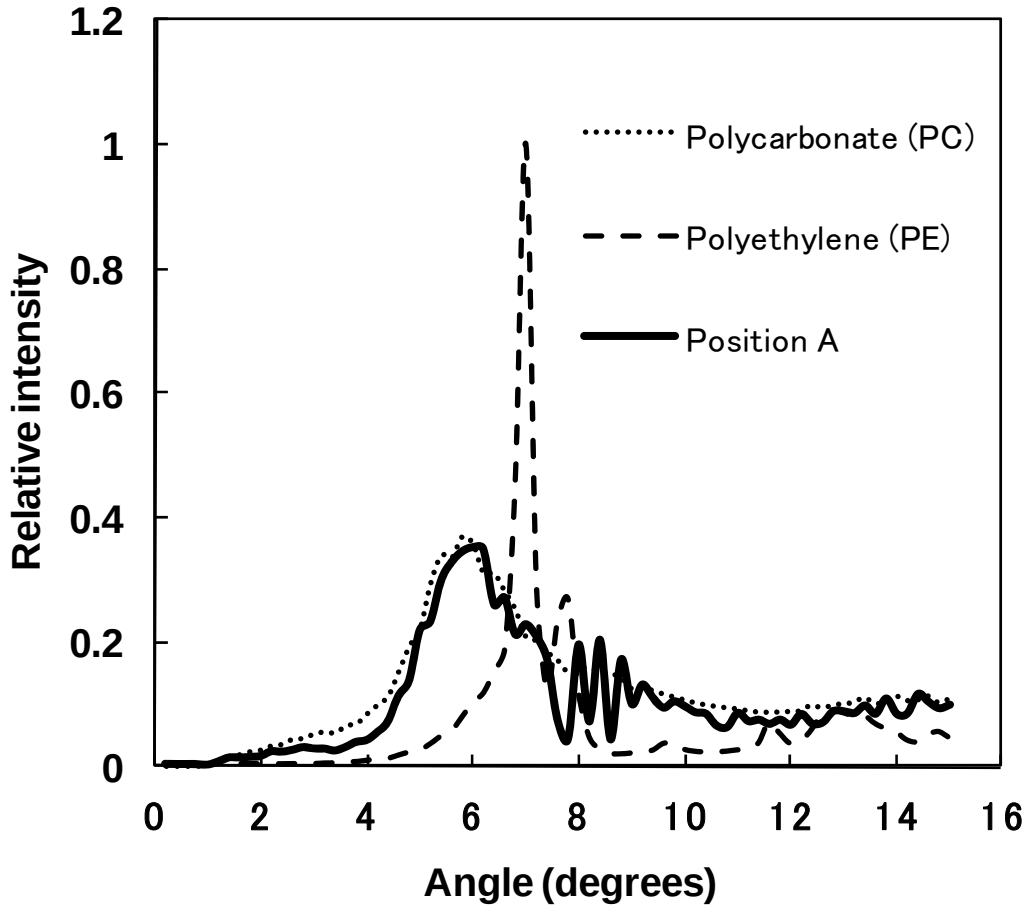
1.2
1
0.8
0.6
0.4
0.2
0
Relative intensity
0
2
4
6
8
10
12
14
16
Angle (degrees)
Polycarbonate (PC)
Polyethylene (PE)
Position A

Fig. 9b

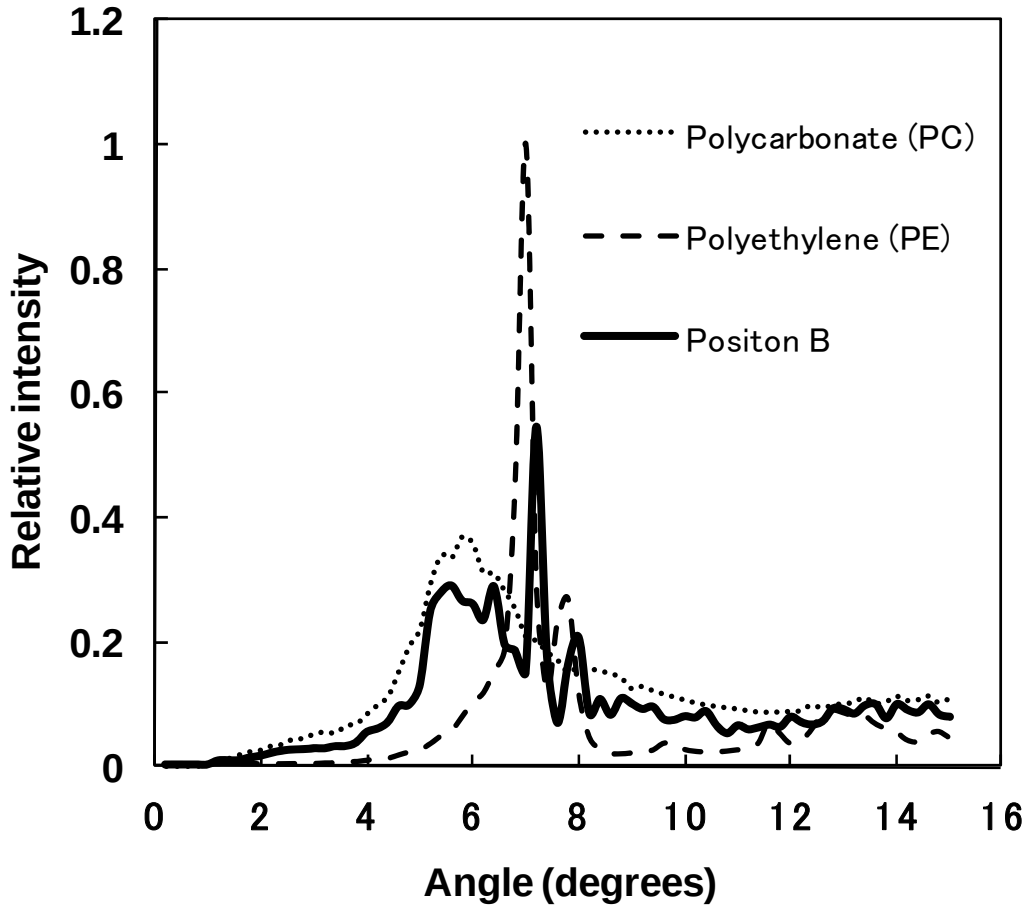
1.2
1
0.8
0.6
0.4
0.2
0
Relative intensity
0
2
4
6
8
10
12
14
16
Angle (degrees)
Polycarbonate (PC)
Polyethylene (PE)
Positon B

Fig. 9c

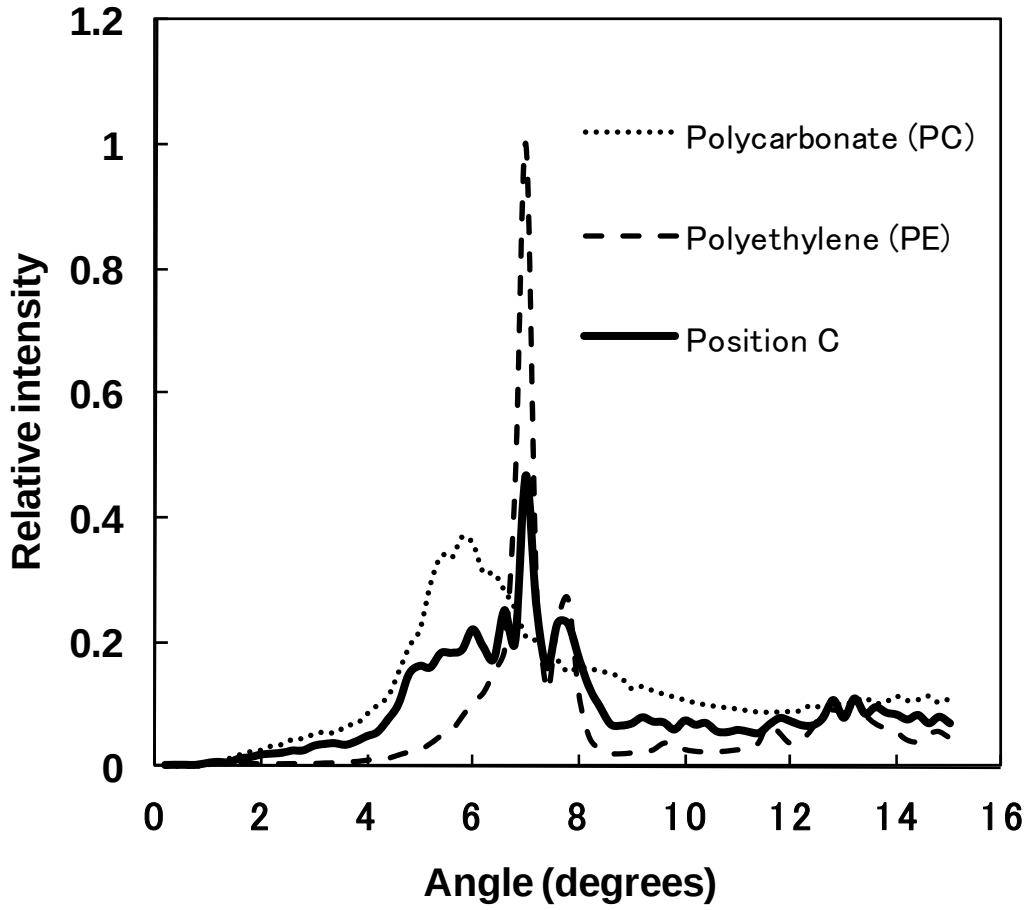
1.2
1
0.8
0.6
0.4
0.2
0
Relative intensity
0
2
4
6
8
10
12
14
16
Angle (degrees)
Polycarbonate (PC)
Polyethylene (PE)
Position C

Fig. 9d

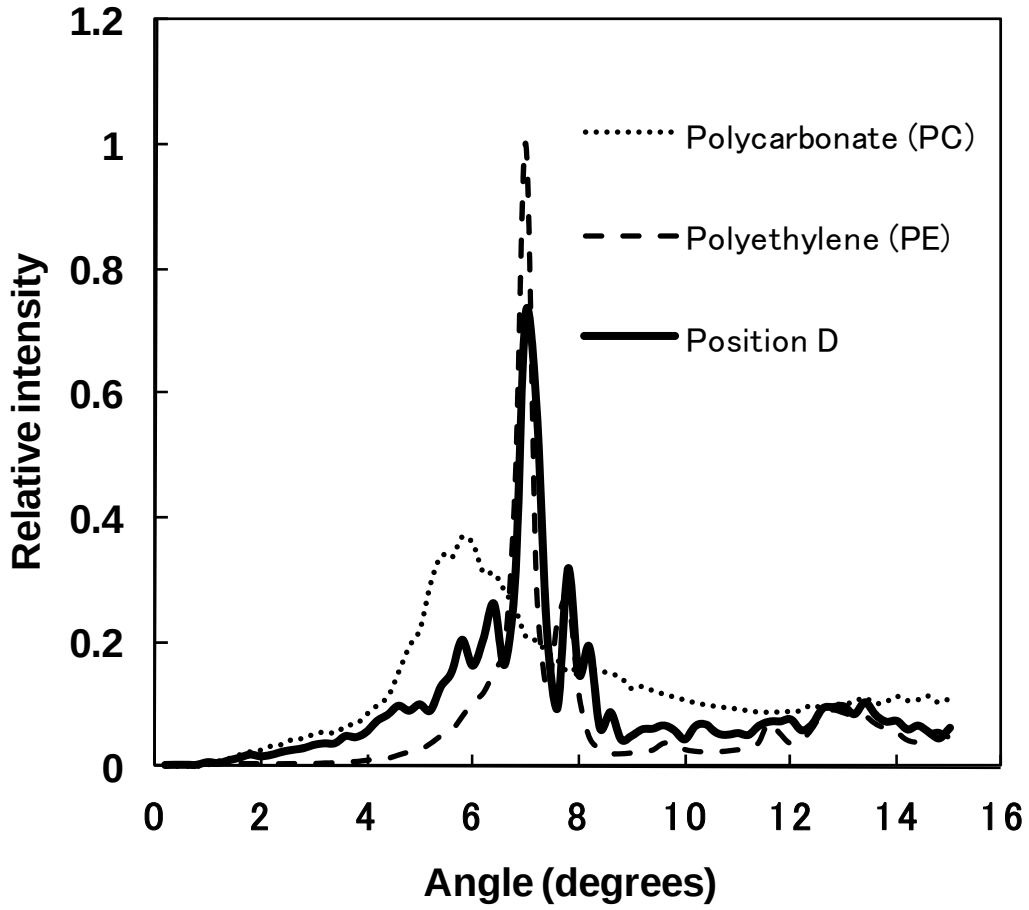
1.2
1
0.8
0.6
0.4
0.2
0
Relative intensity
0
2
4
6
8
10
12
14
16
Angle (degrees)
Polycarbonate (PC)
Polyethylene (PE)
Position D

Fig. 9e

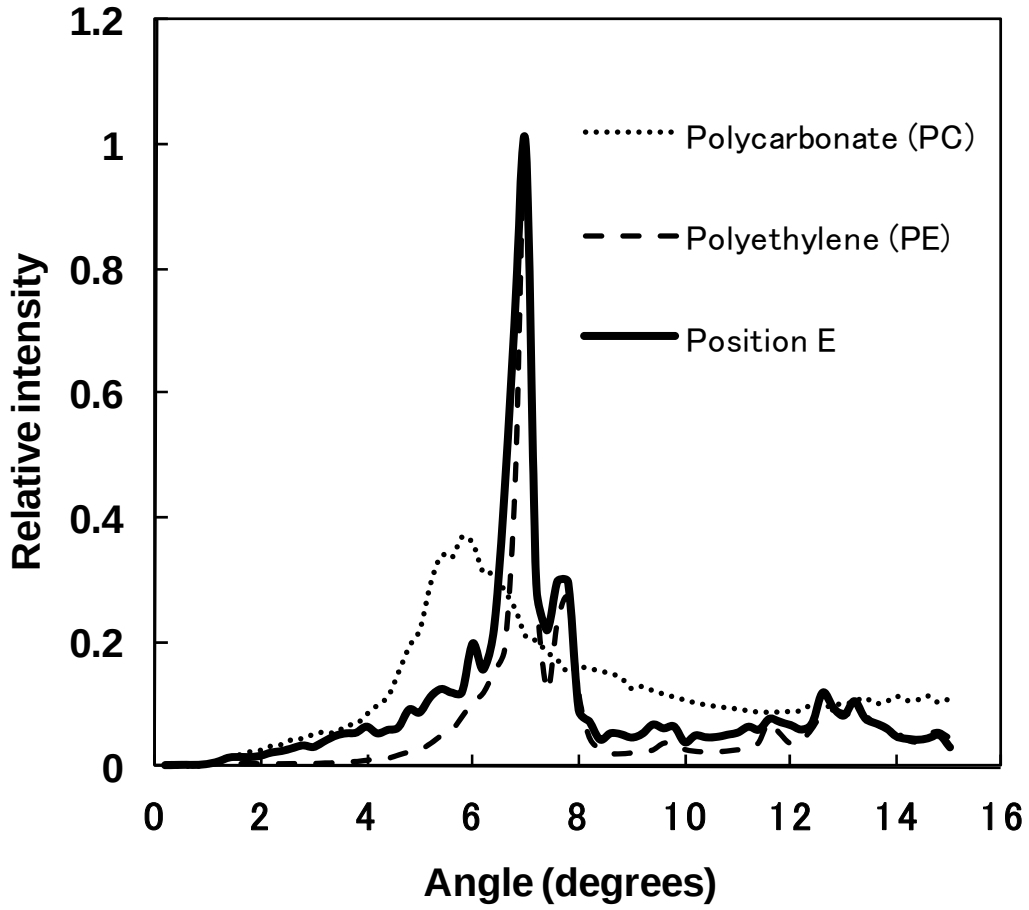
1.2
1
0.8
0.6
0.4
0.2
0
Relative intensity
0
2
4
6
8
10
12
14
16
Angle (degrees)
Polycarbonate (PC)
Polyethylene (PE)
Position E

Fig. 9f

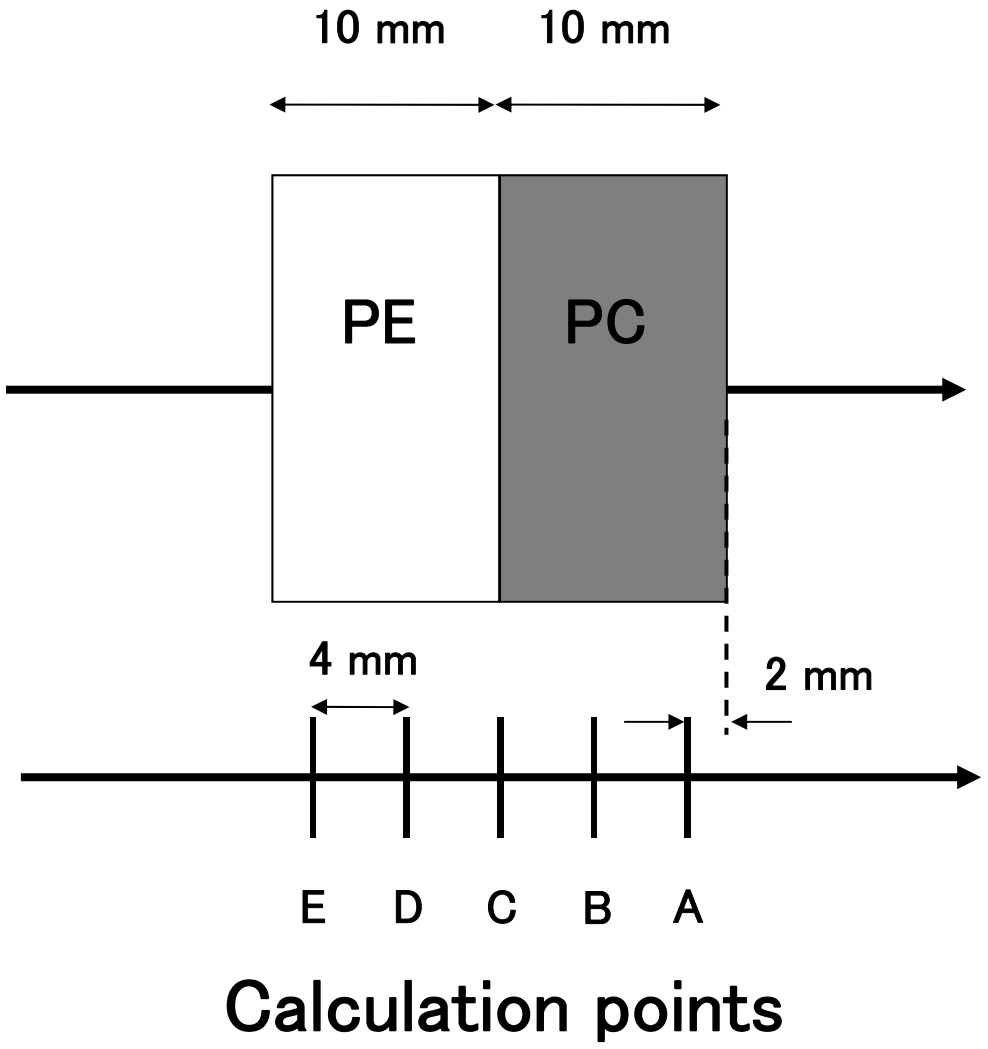

Fig. 9g

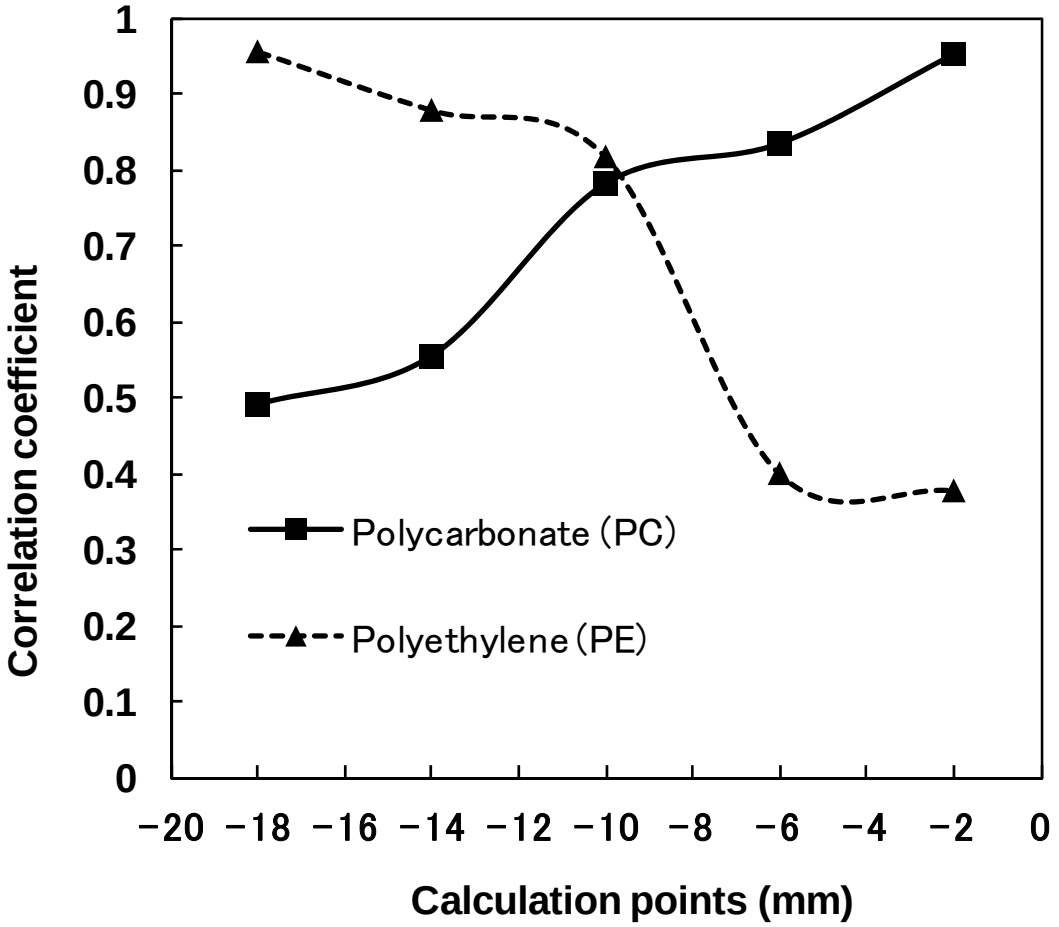
1
0.9
0.8
0.7
0.6
0.5
0.4
0.3
0.2
0.1
0
Correlation coefficient
Polycarbonate (PC)
Polyethylene (PE)
−20 −18 −16 −14 −12 −10 −8 −6 −4 −2 0
Calculation points (mm)

Fig. 10a

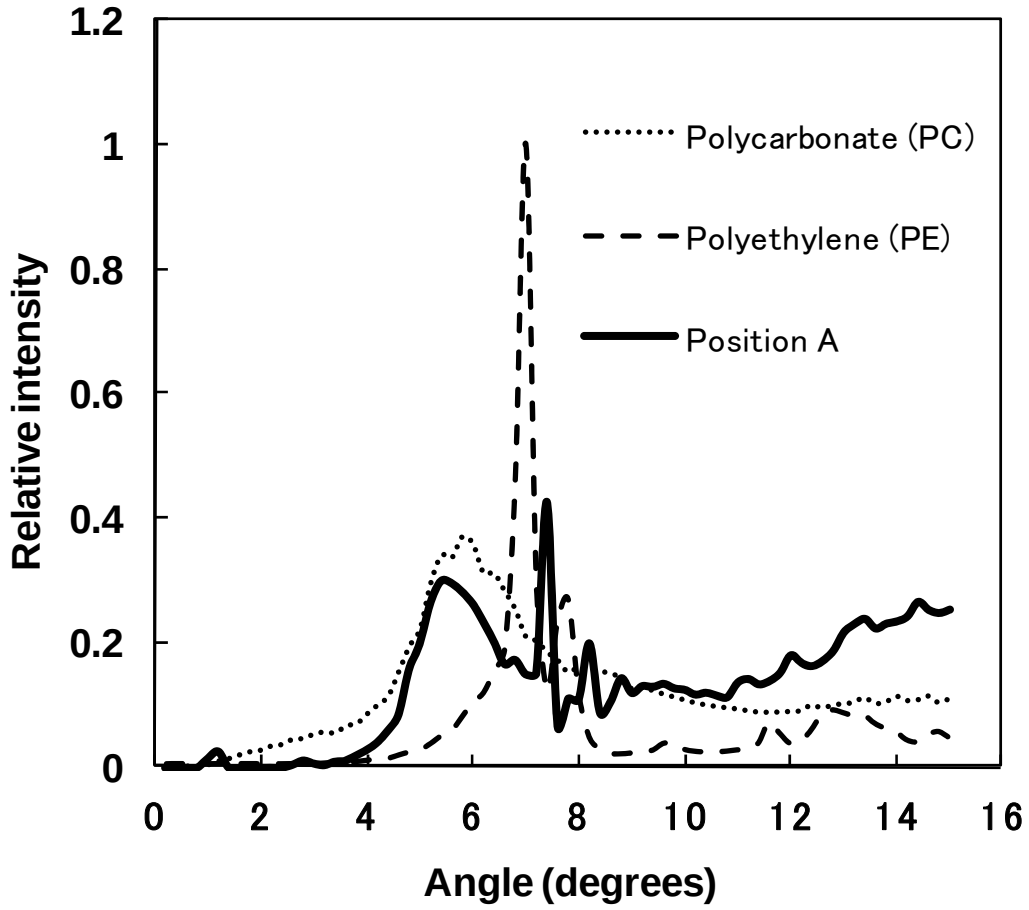
1.2
1
0.8
0.6
0.4
0.2
0
Relative intensity
0
2
4
6
8
10
12
14
16
Angle (degrees)
Polycarbonate (PC)
Polyethylene (PE)
Position A

Fig. 10b

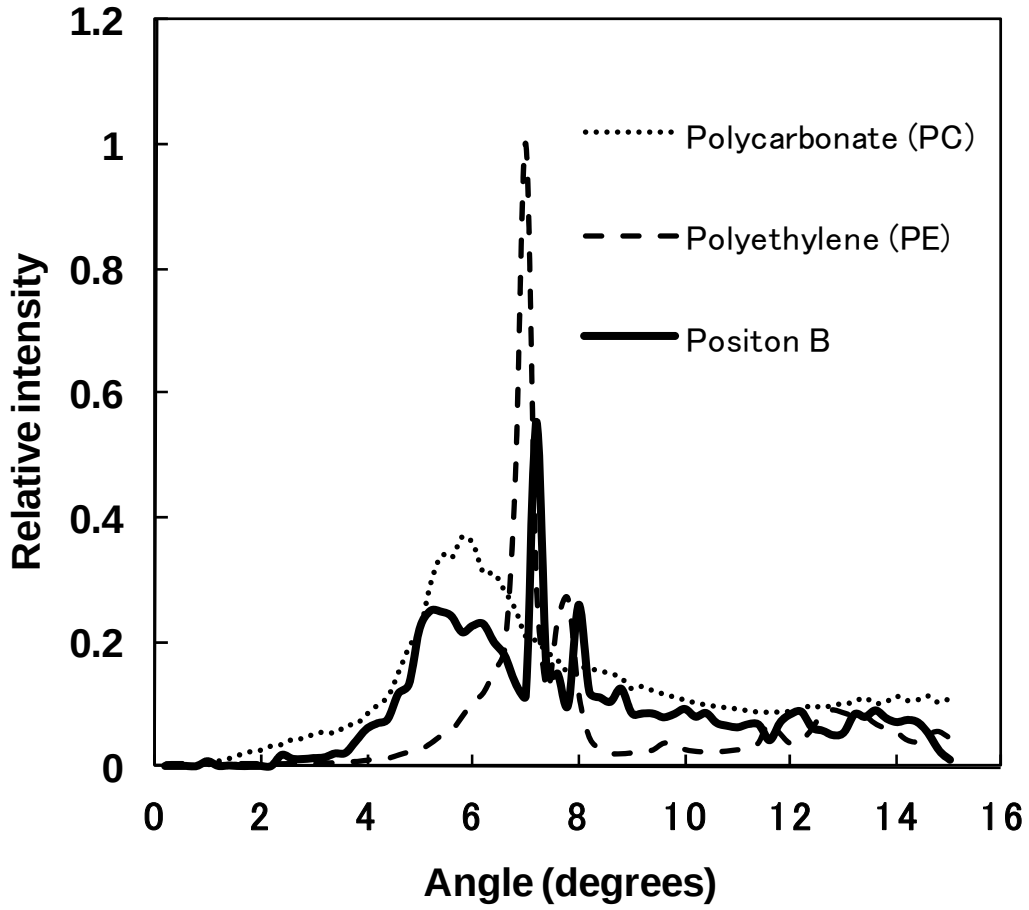
1.2
1
0.8
0.6
0.4
0.2
0
Relative intensity
0
2
4
6
8
10
12
14
16
Angle (degrees)
Polycarbonate (PC)
Polyethylene (PE)
Positon B

Fig. 10c

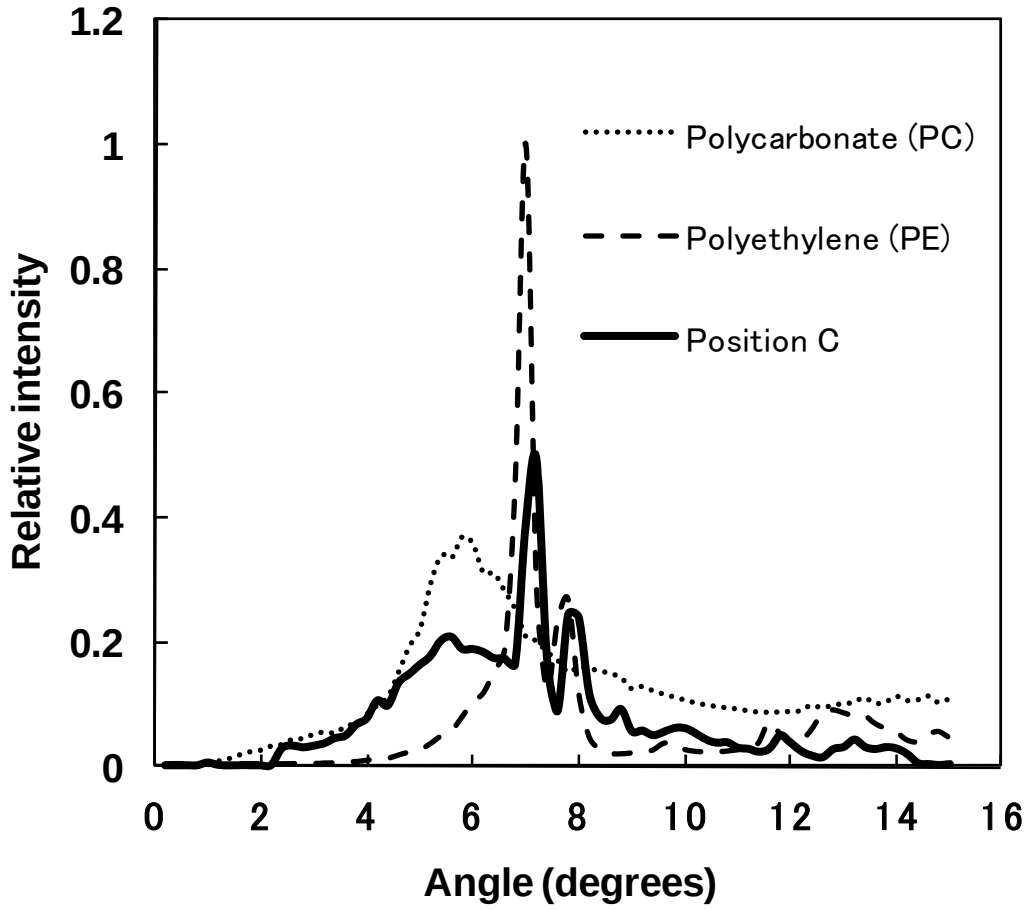
1.2
1
0.8
0.6
0.4
0.2
0
Relative intensity
0
2
4
6
8
10
12
14
16
Angle (degrees)
Polycarbonate (PC)
Polyethylene (PE)
Position C

Fig. 10d

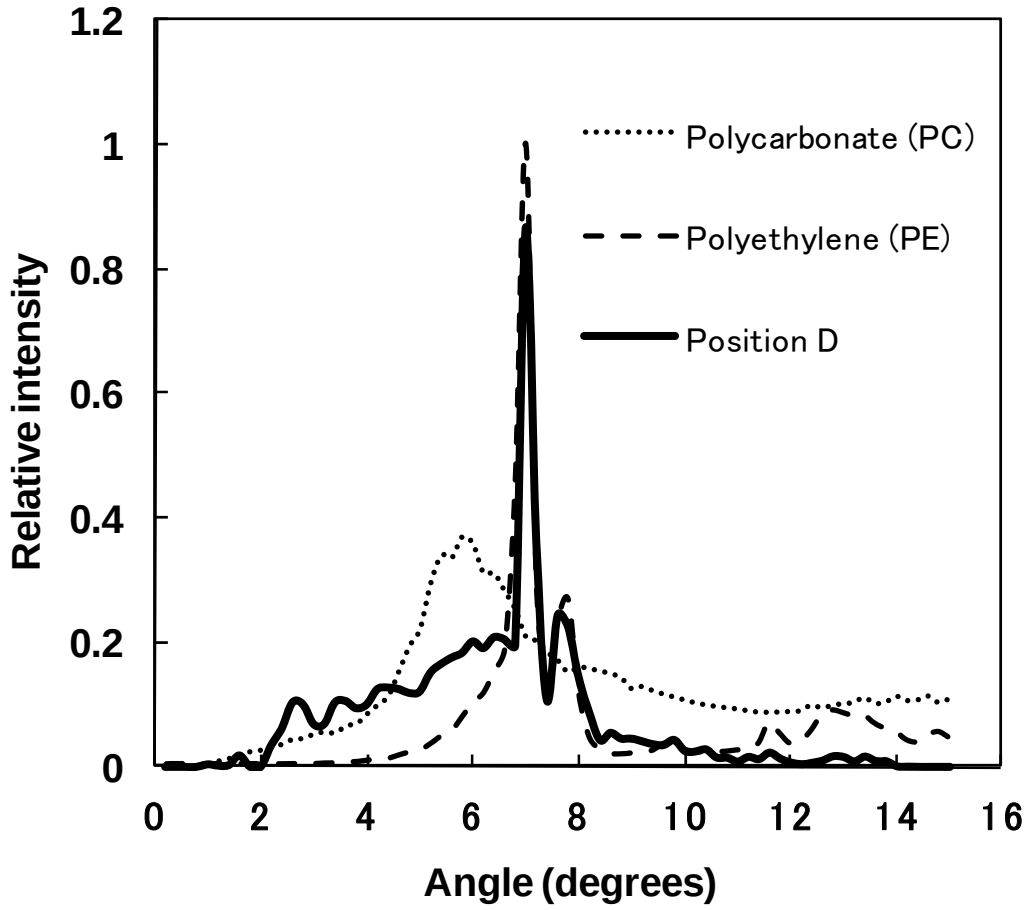
1.2
1
0.8
0.6
0.4
0.2
0
Relative intensity
0
2
4
6
8
10
12
14
16
Angle (degrees)
Polycarbonate (PC)
Polyethylene (PE)
Position D

Fig. 10e

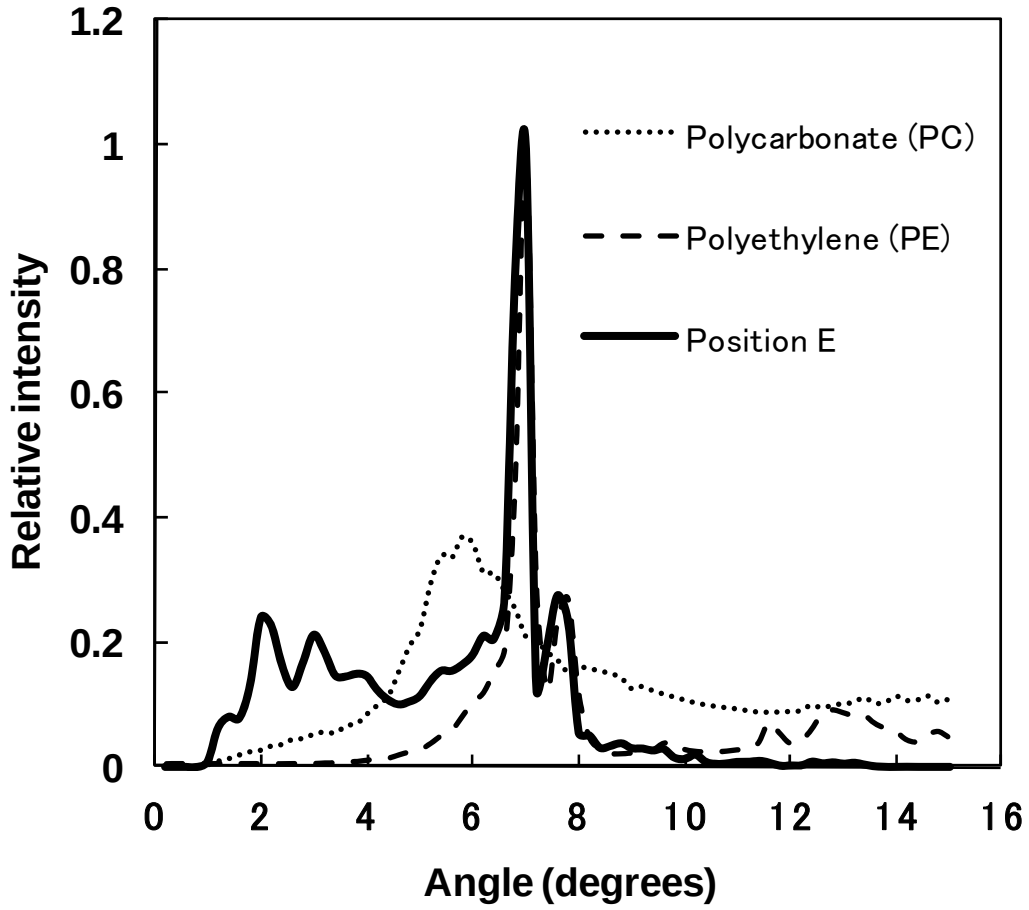
1.2
1
0.8
0.6
0.4
0.2
0
Relative intensity
0
2
4
6
8
10
12
14
16
Angle (degrees)
Polycarbonate (PC)
Polyethylene (PE)
Position E